

Direct Measurement of Three-Dimensional Forces in Atomic Force Microscopy

R. Sri Muthu Mrinalini, R. Sriramshankar, and G. R. Jayanth

Abstract—Direct measurement of three-dimensional (3-D) forces between an atomic force microscope (AFM) probe and the sample benefits diverse applications of AFM, including force spectroscopy, nanometrology, and manipulation. This paper presents the design and evaluation of a measurement system, wherein the deflection of the AFM probe is obtained at two points to enable direct measurement of all the three components of 3-D tip-sample forces in real time. The optimal locations for measurement of deflection on the probe are derived for a conventional AFM probe. Further, a new optimal geometry is proposed for the probe that enables measurement of 3-D forces with identical sensitivity and nearly identical resolution along all three axes. Subsequently, the designed measurement system and the optimized AFM probe are both fabricated and evaluated. The evaluation demonstrates accurate measurement of tip-sample forces with minimal cross-sensitivities. Finally, the real-time measurement system is employed as part of a feedback control system to regulate the normal component of the interaction force, and to perform force-controlled scribing of a groove on the surface of polymethyl methacrylate.

Index Terms—Atomic force microscopy (AFM), direct measurement of 3-D forces, force control, optical beam deflection.

I. INTRODUCTION

THE advent of the atomic force microscope (AFM) [1] has facilitated significant advancements in nanotechnology, in particular, in the fields of atomic resolution imaging, nanometrology, and nanomanipulation [2]–[4]. At the heart of the AFM is a sensitive compliant mechanical probe with a sharply pointed tip that enables highly localized application of forces on a sample. Sensitive detection of the resulting deformation of the mechanical probe facilitates precise force measurement and control. Measurement of the interaction force enables performing force spectroscopy, while regulation of the interaction forces facilitates imaging and controlled manipulation of nanometer-sized entities. Taken together, they have enabled measurement of nanomechanical properties of materials [5], the bond strength of molecules [6], *in situ* imaging of both organic and inorganic samples with molecular resolution or better [7],

and effecting precise surface modifications by means of nanoindentation and nanosurgery [8].

In most of the applications, the AFM is generally employed to interact with nearly planar samples whose surface normal is aligned with that of the tip, i.e., along the Z-axis. This is because the AFM probe possesses maximum sensitivity to tip-sample forces along the Z-axis. Increasingly, however, the AFM is being employed in applications that require interacting with inclined surfaces and three-dimensional (3-D) features, such as in the metrology of trenches and side walls of microfabricated parts [9]–[11] and in manipulation of nanoparticles [12]–[16]. In these applications, where the tip-sample interaction force possesses components along all the three axes, the performance of the AFM is rendered suboptimal for two reasons: First, conventional measurement systems measure components of forces at most along two independent axes. In particular, those forces that act along the length of the probe, viz., the Y-axis, cannot be independently measured from that of the Z-force. Second, by virtue of its structure, a conventional AFM probe possesses significantly lesser sensitivity to both X- and Y-forces compared to Z-forces. These limitations inhibit further innovation leading to more diverse applications of AFM, especially in the fields of metrology and manipulation.

An early attempt [17] to address these limitations employed two laser beams and two photodetectors to measure the deformation at two distinct locations on the probe. This study reported on the measurement of the tip position in 3-D, but not of the tip-sample forces. Subsequent attempts have employed conventional optical beam deflection [18], i.e., with a single laser and photodetector, and have relied on friction models to extract the 3-D forces from the measurements [19]–[21]. Both fixed structure [19], [20] and adaptive [21] models have been investigated. However, these approaches are not applicable when the interaction forces do not originate from friction effects, such as in molecular force spectroscopy or in 3-D nanometrology.

This paper reports the design and evaluation of an optical beam deflection-based measurement system that enables direct measurement of 3-D tip-sample forces, without regard to the origin of the tip-sample interaction forces. The system employs two laser beams along with a single photodetector to measure the deformation of the probe at two distinct points and employ them to measure 3-D tip-sample forces. The optimal locations of the two measurement points that minimize the effect of measurement noise are obtained for a conventional probe. Subsequently, an optimal geometry is proposed for the probe to achieve identical sensitivity and nearly identical resolution in the measured force along all three axes. Next, the measurement system, including the optical system and the optimized AFM

Manuscript received May 9, 2014; revised August 23, 2014 and October 15, 2014; accepted October 24, 2014. Date of publication November 24, 2014; date of current version August 24, 2015. Recommended by Technical Editor Dr. G. Cherubini. This work was supported in part by the Department of Science and Technology under Grant DST 1090.

R. Sri Muthu Mrinalini and R. Sriramshankar are with the Department of Instrumentation and Applied Physics, Indian Institute of Science, Bangalore 560012, India (e-mail: mrinalini@iap.iisc.ernet.in; sriramshankar@iap.iisc.ernet.in).

G. R. Jayanth is with the Department of Instrumentation and Applied Physics and Applied Photonics Initiative, Indian Institute of Science, Bangalore 560012, India (e-mail: jayanth@isu.iisc.ernet.in).

Color versions of one or more of the figures in this paper are available online at <http://ieeexplore.ieee.org>.

Digital Object Identifier 10.1109/TMECH.2014.2366794

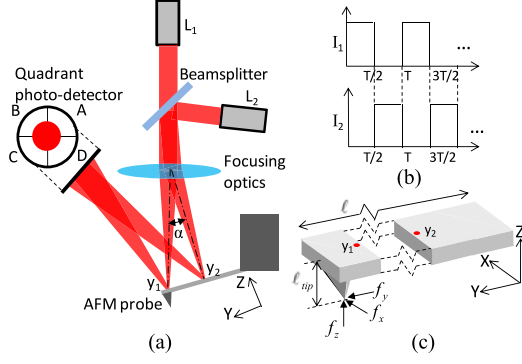


Fig. 1. Schematics showing (a) the construction of the proposed measurement system, (b) the proposed pulsing strategy for the laser beams, and (c) an AFM probe experiencing 3-D tip-sample forces.

probe, are fabricated and calibrated. The developed system is employed to demonstrate independent measurement of all the three components of tip-sample forces. Finally, the measured Z-component of the tip-sample force is employed as part of a feedback control system to regulate the force while scanning a sample, and to perform force-controlled scribing of a groove on the surface of polymethyl methacrylate (PMMA). Compared to the previously reported system for two-point measurement [17], this paper employs a different design, and is devoted to previously unaddressed topics in two-point measurement, including real-time measurement of 3-D forces, optimization of the measurement system, experimental demonstration of 3-D force measurement and its control.

The rest of the paper is divided as follows: Section II describes the design and optimization of the measurement system. Section III describes the fabrication and experimental evaluation of the developed measurement system. Conclusion is presented in Section IV.

II. DESIGN AND OPTIMIZATION OF THE MEASUREMENT SYSTEM

A. Principle of Measurement

Fig. 1(a) depicts the proposed optical beam deflection-based measurement system for measurement of 3-D tip-sample forces. The proposed system comprises of two laser sources L_1 and L_2 whose beams are focused at two distinct locations y_1 and y_2 on the AFM probe, and a single quadrant photodetector that collects the beams after reflection from the AFM probe. The angular separation α between the optical beams is ensured to be small, so that the reflected beams form nearly colocated spots on the photodetector. When the probe experiences tip-sample forces, the resulting small angular deformations at the two locations deflect both the beams and displace their respective spots on the photodetector. These displacements are measured to infer the forces acting at the tip. To measure both the displacements independently, the intensities of the two sources I_1 and I_2 are pulsed with time period T such that only one of them is switched on at any given time [see Fig. 1(b)], and the outputs of the photodetector during this time yield the displacement of the corresponding spot on the detector. This arrangement en-

ables measurement of angular deformations at the two locations on the probe with minimal modification to the existing measurement system. Furthermore, pulsing the lasers at frequencies higher than the resonant frequency of an AFM probe enables measurement of angular deformations due to both quasi-static and dynamic tip-sample interaction forces. However, it is worth noticing that, in practice, the wavelength of the pulsed lasers and the pulsing period T are to be chosen to minimize undesired photothermal effects [22].

Labeling the output voltages of the four quadrants of the photodetector [see Fig. 1(a)] as V_A , V_B , V_C , and V_D , it is seen that the signal $V_y = V_A + V_B - (V_C + V_D)$ is proportional to the angular deformation θ_x of the probe about the X-axis at the site of measurement, while the signal $V_x = V_A + V_D - (V_B + V_C)$ is proportional to the angular deformation θ_y of the probe about the Y-axis. Thus, the outputs $V_x(y_i)$, $V_y(y_i)$ at the two measurement locations y_i ($i = 1, 2$) are related to the corresponding angular deformations $\theta_y(y_i)$, $\theta_x(y_i)$ as

$$\begin{bmatrix} V_x(y_i) \\ V_y(y_i) \end{bmatrix} = \begin{bmatrix} 0 & k_{phy}(y_i) \\ k_{phx}(y_i) & 0 \end{bmatrix} \begin{bmatrix} \theta_x(y_i) \\ \theta_y(y_i) \end{bmatrix} \quad (1)$$

where $k_{phx}(y_i)$, $k_{phy}(y_i)$ represent the sensitivities of the measurement system to angular deformations at the location y_i ($i = 1, 2$).

For an AFM probe deforming under the influence of quasi-static tip-sample interaction forces [see Fig. 1(c)], the angular deformations $\theta_y(y_i)$ result from the X-axis force f_x experienced by the tip and are given by

$$\theta_y(y_i) = c_{\theta x}(y_i) f_x \quad (2)$$

where the angular compliances $c_{\theta x}(y_i)$ are obtained from Saint-Venant theory [23, pp. 289–290], and are given by

$$c_{\theta x}(y_i) = - \int_0^{y_i} \frac{\ell_{\text{tip}}}{GJ(y)} dy. \quad (3)$$

In (3), ℓ_{tip} represents the height of the tip, J represents the torsional constant, and G represents the shear modulus of the probe.

Likewise, the angular deformations $\theta_x(y_i)$ result from Z-axis force f_z and Y-axis force f_y acting at the tip. In the presence of both the forces, the resulting angular deformations $\theta_x(y_i)$ are the sum of both their effects, and are given by

$$\theta_x(y_i) = c_{\theta y}(y_i) f_y + c_{\theta z}(y_i) f_z \quad (4)$$

where $c_{\theta y}(y_i)$, $c_{\theta z}(y_i)$ represent the angular compliances of the probe at the locations y_i ($i = 1, 2$) to f_y and f_z , respectively. From Euler–Bernoulli beam theory [23, pp. 137–154], the compliances $c_{\theta y}(y_i)$, $c_{\theta z}(y_i)$ of a slender probe of overall length ℓ are given by

$$\begin{aligned} c_{\theta y}(y_i) &= \int_0^{y_i} \frac{\ell_{\text{tip}}}{EI(y)} dy \\ c_{\theta z}(y_i) &= \int_0^{y_i} \frac{(\ell - y)}{EI(y)} dy \end{aligned} \quad (5)$$

where I represents the second moment of inertia of the beam's cross section, and E represents the Young's modulus of the beam.

Employing (2) and (4) it is seen that the three measurements $\theta = [\theta_y(y_1) \ \theta_x(y_1) \ \theta_x(y_2)]^T$ are related to the three components of a 3-D tip-sample force $\mathbf{f} = [f_x \ f_y \ f_z]^T$ as

$$\begin{bmatrix} \theta_y(y_1) \\ \theta_x(y_1) \\ \theta_x(y_2) \end{bmatrix} = \begin{bmatrix} c_{\theta x}(y_1) & 0 & 0 \\ 0 & c_{\theta y}(y_1) & c_{\theta z}(y_1) \\ 0 & c_{\theta y}(y_2) & c_{\theta z}(y_2) \end{bmatrix} \begin{bmatrix} f_x \\ f_y \\ f_z \end{bmatrix} = \mathbf{C}_\theta \mathbf{f}. \quad (6)$$

Thus, (6) can be employed to obtain the force f_x from the angular deformation $\theta_y(y_1)$, while the forces f_y and f_z can be independently obtained from the measurements $\theta_x(y_1)$ and $\theta_x(y_2)$ provided $c_{\theta y}(y_1)/c_{\theta z}(y_1) \neq c_{\theta y}(y_2)/c_{\theta z}(y_2)$. Taken together, a 3-D force $\mathbf{f} = [f_x \ f_y \ f_z]^T$ can be obtained from the three measurements $\theta = [\theta_y(y_1) \ \theta_x(y_1) \ \theta_x(y_2)]^T$ as

$$\mathbf{f} = \mathbf{C}_\theta^{-1} \theta. \quad (7)$$

B. Optimization of the Measurement System

While (7) indicates that measurement of the probe deformation at any two points y_i ($i = 1, 2$) enables obtaining all the three components of 3-D force \mathbf{f} , in the presence of measurement noise, the accuracy of the measurements of force would depend on the specific choice of the two points. If $\theta_n = [\theta_{y1n} \ \theta_{x1n} \ \theta_{x2n}]^T$ represents the noise in the three angular measurements, the corresponding noise in the obtained force $\mathbf{f}_n = [f_{xn} \ f_{yn} \ f_{zn}]^T$ is given by $\mathbf{f}_n = \mathbf{C}_\theta^{-1} \theta_n$. Assuming that all the three elements of θ_n are mutually uncorrelated sources of the Gaussian white noise with zero mean and a standard deviation σ_θ , the standard deviation of noise in force measurements [24] along the X-, Y- and Z-axes, viz., σ_{fx} , σ_{fy} , σ_{fz} , respectively, are given by

$$\begin{aligned} \sigma_{fx} &= \frac{\sigma_\theta}{|c_{\theta x}(y_1)|} \\ \sigma_{fy} &= \frac{\sigma_\theta \sqrt{c_{\theta z}^2(y_1) + c_{\theta z}^2(y_2)}}{|c_{\theta y}(y_1)c_{\theta z}(y_2) - c_{\theta y}(y_2)c_{\theta z}(y_1)|} \\ \sigma_{fz} &= \frac{\sigma_\theta \sqrt{c_{\theta y}^2(y_1) + c_{\theta y}^2(y_2)}}{|c_{\theta y}(y_1)c_{\theta z}(y_2) - c_{\theta y}(y_2)c_{\theta z}(y_1)|}. \end{aligned} \quad (8)$$

This section analyzes the optimal locations y_i ($i = 1, 2$) that minimize σ_{fx} , σ_{fy} , and σ_{fz} for conventional rectangular AFM probes. Subsequently, optimization of the geometry of the probe itself such that the effect of measurement noise is reduced further is described.

1) *Optimization of the Measurement Locations for Conventional AFM Probes:* For a conventional AFM probe with uniform cross section, the compliances $c_{\theta x}(y_i)$, $c_{\theta y}(y_i)$, and $c_{\theta z}(y_i)$, obtained from (3) and (5), are given by

$$c_{\theta x}(y_i) = -\frac{\ell_{\text{tip}} y_i}{GJ}$$

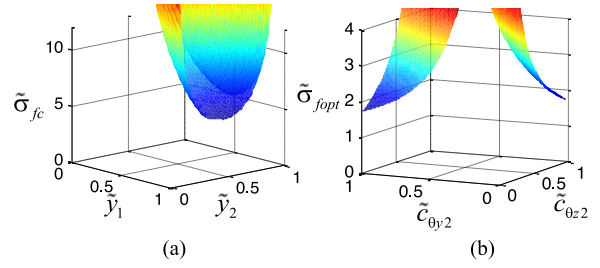


Fig. 2. Plots of (a) $\tilde{\sigma}_{fc}$ as function of \tilde{y}_1, \tilde{y}_2 for the conventional probe and (b) $\tilde{\sigma}_{fopt}$ as function of $\tilde{c}_{\theta z2}, \tilde{c}_{\theta y2}$ for a probe with specialized geometry.

$$\begin{aligned} c_{\theta y}(y_i) &= \frac{\ell_{\text{tip}} y_i}{EI} \\ c_{\theta z}(y_i) &= \frac{1}{EI} \left(\ell y_i - \frac{y_i^2}{2} \right). \end{aligned} \quad (9)$$

Equation (9) can be used along with (8) to obtain σ_{fx} , σ_{fy} , and σ_{fz} as functions of $\tilde{y}_1 = y_1/\ell$, $\tilde{y}_2 = y_2/\ell$, and are given by

$$\begin{aligned} \sigma_{fx} &= \frac{GJ}{\ell \ell_{\text{tip}} \tilde{y}_1} \sigma_\theta \\ \sigma_{fy} &= \frac{2EI}{\ell \ell_{\text{tip}}} \frac{\sqrt{\tilde{y}_1^2(1 - \tilde{y}_1/2)^2 + \tilde{y}_2^2(1 - \tilde{y}_2/2)^2}}{[\tilde{y}_1 \tilde{y}_2 (\tilde{y}_1 - \tilde{y}_2)]} \sigma_\theta \\ \sigma_{fz} &= \frac{2EI}{\ell^2} \frac{\sqrt{\tilde{y}_1^2 + \tilde{y}_2^2}}{[\tilde{y}_1 \tilde{y}_2 (\tilde{y}_1 - \tilde{y}_2)]} \sigma_\theta. \end{aligned} \quad (10)$$

It is seen from (10) that σ_{fx} achieves the smallest value for $\tilde{y}_1 = 1$ or equivalently $y_1 = \ell$. To ensure small values of σ_{fy} and σ_{fz} , the corresponding optimal values of \tilde{y}_1, \tilde{y}_2 are obtained by minimizing a cost function defined as

$$\tilde{\sigma}_{fc}(\tilde{y}_1, \tilde{y}_2) = \sqrt{\tilde{\sigma}_{fy}^2(\tilde{y}_1, \tilde{y}_2) + \tilde{\sigma}_{fz}^2(\tilde{y}_1, \tilde{y}_2)} \quad (11)$$

where $\tilde{\sigma}_{fy} = [\ell \ell_{\text{tip}} / 2EI \sigma_\theta] \sigma_{fy}$ and $\tilde{\sigma}_{fz} = [\ell^2 / 2EI \sigma_\theta] \sigma_{fz}$. Fig. 2(a) plots $\tilde{\sigma}_{fc}$ as function of \tilde{y}_1, \tilde{y}_2 and shows that $\tilde{\sigma}_{fc}$ reaches its minimum value for $\tilde{y}_1 = 1$ and $\tilde{y}_2 \approx 0.46$. Thus, choosing $y_1 = \ell$ and $y_2 \approx 0.5 \ell$ enables achieving the least noise in measurement of both Y- and Z-axes forces.

For a probe of rectangular cross section, with width w and thickness t ($t \ll w$), it is noted that $J = wt^3/3$ and $I = wt^3/12$. Designating $c_{\theta z}(\ell) = S$, the resulting minimum standard deviations in the noise along the three axes are obtained for the probe in terms of S, ℓ , and ℓ_{tip} as

$$\begin{aligned} \sigma_{fx \min} &= [2G\ell/E\ell_{\text{tip}}] \sigma_\theta / S \\ \sigma_{fy \min} &= [2.47\ell/\ell_{\text{tip}}] \sigma_\theta / S \\ \sigma_{fz \min} &= 4.43 \sigma_\theta / S. \end{aligned} \quad (12)$$

Since the standard deviation of the noise in Z-force measurement, in the absence of Y-force, is given by $\sigma_{fz} = \sigma_\theta / S$, it is seen that in the presence of Y-force, the standard deviation of the noise is enhanced by over four times. Furthermore, it is evident from (12) that $\sigma_{fx \min} / \sigma_{fz \min} = [0.45 G/E] \ell / \ell_{\text{tip}}$ while $\sigma_{fy \min} / \sigma_{fz \min} = 0.56 \ell / \ell_{\text{tip}}$. Since $\ell / \ell_{\text{tip}} \sim 10-15$ for a conventional probe, the minimum standard deviation of the

noise in X - and Y -forces are significantly higher than that of the Z -force.

2) *Optimization of the Geometry of the Probe to Minimize the Effect of Measurement Noise:* The difference in the effects of measurement noise on the measured forces along X -, Y - and Z -axes arise from the significantly lower sensitivity of a conventional probe to X - and Y -forces compared to Z -force. This, in turn, is a consequence of the uniform geometry of the rectangular probe. Thus, this section considers a nonuniform geometry for the probe such that it results in identical angular sensitivities S to tip-sample forces along the three axes at the measurement location near the tip (y_1), i.e.,

$$|c_{\theta x}(y_1)| = c_{\theta y}(y_1) = c_{\theta z}(y_1) = S. \quad (13)$$

Next, the compliances $c_{\theta y}(y_2)$, $c_{\theta z}(y_2)$ are determined such that they minimize the effect of measurement noise on the measurements of f_y, f_z . Finally, the geometry of the probe that enables realization of the optimal compliances is obtained.

Using (13) along with (8), the standard deviations of noise in force measurements along the three axes for a general nonuniform probe are given by

$$\begin{aligned} \sigma_{fx} &= \sigma_{\theta}/S \\ \sigma_{fy} &= \sigma_{\theta} \sqrt{1 + \tilde{c}_{\theta z 2}^2 / [S(\tilde{c}_{\theta z 2} - \tilde{c}_{\theta y 2})]} \\ \sigma_{fz} &= \sigma_{\theta} \sqrt{1 + \tilde{c}_{\theta y 2}^2 / [S(\tilde{c}_{\theta z 2} - \tilde{c}_{\theta y 2})]} \end{aligned} \quad (14)$$

where $\tilde{c}_{\theta y 2} = c_{\theta y}(y_2)/S$ and $\tilde{c}_{\theta z 2} = c_{\theta z}(y_2)/S$. It is evident from (14) that σ_{fx} is determined by σ_{θ} and S alone, while σ_{fy}, σ_{fz} are also determined by the compliances $c_{\theta z}(y_2), c_{\theta y}(y_2)$. To minimize the effects of $\tilde{c}_{\theta z 2}, \tilde{c}_{\theta y 2}$ on the measurement noise in both Y - and Z -force measurements, a cost function $\tilde{\sigma}_{f_{opt}}$ is defined, which is given by

$$\tilde{\sigma}_{f_{opt}}(\tilde{c}_{\theta z 2}, \tilde{c}_{\theta y 2}) = \sqrt{\tilde{\sigma}_{fy}^2(\tilde{c}_{\theta z 2}, \tilde{c}_{\theta y 2}) + \tilde{\sigma}_{fz}^2(\tilde{c}_{\theta z 2}, \tilde{c}_{\theta y 2})}. \quad (15)$$

where $\tilde{\sigma}_{fy} = \sigma_{fy}S/\sigma_{\theta}$ and $\tilde{\sigma}_{fz} = \sigma_{fz}S/\sigma_{\theta}$. Fig. 2(b) plots $\tilde{\sigma}_{f_{opt}}$ as function of $\tilde{c}_{\theta z 2}, \tilde{c}_{\theta y 2}$ for $0 \leq \tilde{c}_{\theta y 2}, \tilde{c}_{\theta z 2} \leq 1$ and shows that $\tilde{\sigma}_{f_{opt}}$ attains its minimum value for two cases, viz., $\tilde{c}_{\theta y 2} = 1, \tilde{c}_{\theta z 2} = 0$ and $\tilde{c}_{\theta y 2} = 0, \tilde{c}_{\theta z 2} = 1$.

Thus, the design of the probe is performed to ensure that $\tilde{c}_{\theta z 2}, \tilde{c}_{\theta y 2}$ are close to any one of the two limits and accordingly, the corresponding limits for the dimensions of the probe are derived. Here, the limit is chosen to be $\tilde{c}_{\theta y 2} \rightarrow 0$ and $\tilde{c}_{\theta z 2} \rightarrow 1$ or equivalently, $c_{\theta y}(y_2) \rightarrow 0$ and $c_{\theta z}(y_2) \rightarrow S$. Fig. 3 is a schematic showing a probe possessing nonuniform geometry, with overall length ℓ and tip height ℓ_{tip} . If the two measurement points y_1 and y_2 divide the probe into the three regions of lengths ℓ_0, ℓ_1 , and ℓ_2 , it is assumed here that each of these regions are cantilever beams with uniform cross section and second moments of inertia I_i ($i = 0, 1, 2$). The terms $c_{\theta y}(y_i), c_{\theta z}(y_i)$ can be written in terms of ℓ_i and I_i ($i = 0, 1, 2$) by employing (5), and are given by

$$c_{\theta z}(y_1) = S = \frac{\ell_1^2}{2EI_1} + \frac{\ell_2^2}{2EI_2} + \frac{\ell_0\ell_1}{EI_1} + \frac{(\ell_0 + \ell_1)\ell_2}{EI_2} \quad (16)$$

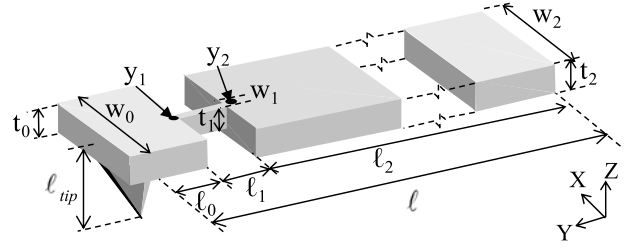


Fig. 3. Schematic of a nonuniform AFM probe comprised of three regions, each with uniform cross section, separated by the two measurement points y_1 and y_2 .

$$c_{\theta z}(y_2) = \frac{\ell_2^2}{2EI_2} + \frac{(\ell_0 + \ell_1)\ell_2}{EI_2} \quad (17)$$

$$c_{\theta y}(y_1) = \frac{\ell_{tip}\ell_1}{EI_1} + \frac{\ell_{tip}\ell_2}{EI_2} \quad (18)$$

$$c_{\theta y}(y_2) = \frac{\ell_{tip}\ell_2}{EI_2}. \quad (19)$$

Subtracting (17) from (16) and noting that for the optimal probe $c_{\theta z}(y_2) \rightarrow S$, it is seen that

$$\frac{\ell_1}{EI_1} \left(\ell_0 + \frac{\ell_1}{2} \right) \rightarrow 0. \quad (20)$$

Likewise, subtracting (19) from (18) and employing the fact that $c_{\theta y}(y_2) \rightarrow 0$, it is seen that

$$\frac{\ell_{tip}\ell_1}{EI_1} \rightarrow S. \quad (21)$$

Since it is evident from (21) that $\ell_1/EI_1 \rightarrow S/\ell_{tip}$, (20) can be used to deduce that $(\ell_0 + \ell_1/2) \rightarrow 0$, or equivalently, $\ell_0 \rightarrow 0$ and $\ell_1 \rightarrow 0$. This implies that $\ell_2 \rightarrow \ell$. Finally, from (16), it can be concluded that $\ell_2^2/2EI_2 \rightarrow S$.

While the optimal limits cannot be exactly realized in practice, they can be employed to guide the design of a nonuniform probe such that its compliances are nearly optimal. It is assumed that each of the three regions possess rectangular cross sections of width w_i and thickness t_i ($i = 0, 1, 2$), so that their second moments of inertia are given by $I_i = w_i t_i^3/12$. First, the limit $\ell_0 \rightarrow 0$ indicates that in practice, the longitudinal offset between y_1 and the tip is required to be as small as possible. Since $\ell_2 \approx \ell$, the condition $c_{\theta z}(y_2) = 6\ell_2^2/Ew_2t_2^3 \rightarrow S$ can be employed to determine the dimensions w_2, t_2 . Subsequently, the length ℓ_1 is chosen such that $\ell_1 \ll \ell_2$, and the condition $c_{\theta y}(y_1) = 12\ell_{tip}\ell_1/Ew_1t_1^3 \rightarrow S$ is employed to determine the dimensions w_1, t_1 . Finally, the chosen dimensions are verified to satisfy the condition $c_{\theta y}(y_2) \ll c_{\theta y}(y_1)$, or equivalently

$$w_1 t_1^3 \ll \frac{\ell_1}{\ell_2} w_2 t_2^3. \quad (22)$$

In general, it can be seen that (22) is satisfied when $w_1 \ll w_2$ and $t_1 \ll t_2$. Thus, realization of the optimal compliances results in a probe geometry, wherein the two-measurement points are situated close to the tip and are separated by a region that is relatively short and slender compared to the rest of the probe.

The noise in measurement of Y - and Z -forces for the optimal probe are $\sigma_{fy} = \sigma_\theta \sqrt{2}/S$ and $\sigma_{fz} = \sigma_\theta/S$. In combination with the fact that $\sigma_{fx} = \sigma_\theta/S$, it is seen that the optimal geometry for the probe results in nearly identical noise in force measurements along all the three axes, with their magnitudes being on the order of σ_θ/S . In comparison with the measurement noise for a conventional probe with identical Z -force sensitivity and $\ell/\ell_{tip} \sim 10$ [see (12)], it is seen that the optimal design results in over ten times lesser noise in force measurements along X - and Y -axes and over four times lesser noise along the Z -axis.

III. DIRECT MEASUREMENT OF 3-D TIP-SAMPLE FORCES: SYSTEM DEVELOPMENT AND EVALUATION

The measurement system proposed in Section II was designed, fabricated, and evaluated. Section III-A describes the design and fabrication of the measurement system. Section III-B describes the evaluation of the measurement system for determination of 3-D forces. Finally, in Section III-C, the use of the measured force as part of a feedback control system to regulate the Z -axis component of tip-sample force in real time is described.

A. Design and Fabrication of the Measurement System

The 3-D force measurement system comprises of the optical beam-deflection system and an AFM probe that deforms in response to tip-sample forces. The design and fabrication of the optical system is described first, followed by that of the optimized AFM probe.

1) *Design and Fabrication of the Optical System:* The optical system comprises of two laser sources, a stereo-microscope, a quadrant photodetector and associated electronics [see Fig. 4(a)]. The two laser sources (5 mW, 630-nm laser diodes) were mounted within a fixture such that their beams were directed into one of the eyepieces of the stereo microscope (SZ61 TR, Olympus). The other eyepiece was employed to view the focused spots, the AFM probe, and the sample. The laser beams reflected from the probe were captured by a quadrant photodetector (QP100-6, First Sensor). The electronic components were employed for pulsing of both the lasers, for performing signal conditioning and for data acquisition. The construction of the fixture for the two sources and the electronics are briefly described.

Fig. 4(b) shows the cross section of the fixture employed to position the laser sources over the eyepiece. The fixture contained the laser casings, a goniometer, and a beam splitter. The casings and the goniometer enabled changing the relative position and orientations of the two sources, while the beam splitter enabled combining the two beams and directing them into the eyepiece of the microscope. The entire unit was firmly fixed on the eyepiece by means of four spring-loaded screws. Together, the fixture enabled precise focusing of the two laser beams at any desired location within the field of view of the microscope. Fig. 4(c) shows the photograph of the overall system, while Fig. 4(d) shows a photograph of the fixture. Fig. 4(e) is a micrograph showing the two laser spots focused near the middle and the end of an AFM probe.

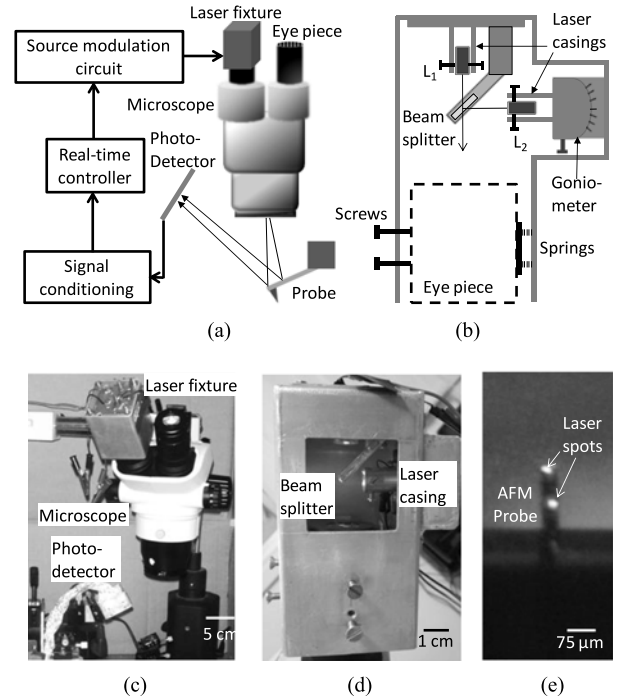


Fig. 4. Schematics showing (a) the important components of the measurement system and (b) cross-sectional view of the fixture employed to mount the laser sources. Photographs showing (c) the overall measurement system, (d) the fixture for the laser sources, and (e) the two laser beams focused on an AFM probe.

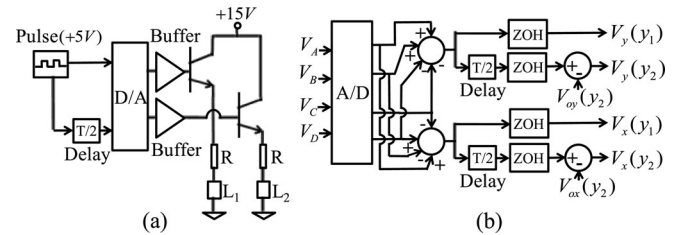


Fig. 5. (a) Schematic of the system employed to pulse the laser sources. The resistors R were chosen such that a current of about 16 mA passed through the laser diodes. Further, the forward current gain of the transistors were about 100. (b) Schematic of the system employed to measure $V_x(y_i)$, $V_y(y_i)$ ($i = 1, 2$). In the figure, ZOH represents a zero-order hold block.

In the developed system, all actions related to actuation, measurement, and control were performed by a real-time controller (DS 1103, dSPACE), where the necessary block diagrams were built using MATLAB Simulink and operated at 2 kHz update rate. Fig. 5(a) shows a schematic of the system employed to pulse the two lasers. The two beams were pulsed by the real-time controller with a period of $T = 4$ ms. The choice of a relatively large time period T was based on the quasi-static nature of the tip-sample forces that were measured in the experiments. The time delay between the two lasers was maintained to be $T/2 = 2$ ms. The corresponding outputs of the four quadrants of the detector, viz., V_A , V_B , V_C , and V_D , were acquired by the same controller and sampled at appropriate time instants so as to read $V_x(y_i)$, $V_y(y_i)$ ($i = 1, 2$). Since the laser beams from y_1 and y_2

TABLE I
DIMENSIONS AND ANGULAR COMPLIANCES OF THE OPTIMIZED PROBE

Dimensions (μm)		
$\ell_0 = 14, w_0 = 35, t_0 = 3$	$\ell_2 = 192.3, w_2 = 35, t_2 = 3$	
$\ell_1 = 7, w_1 = 1.38, t_1 = 1$	$\ell_{\text{tip}} = 14$	
Angular compliances ($\text{mrad}/\mu\text{N}$)		
$c_{\theta x}(y_1) = -6.2$	$c_{\theta y}(y_1) = 5.365$	$c_{\theta z}(y_1) = 8.21$
$c_{\theta x}(y_2) = -0.24$	$c_{\theta y}(y_2) = 0.21$	$c_{\theta z}(y_2) = 1.735$

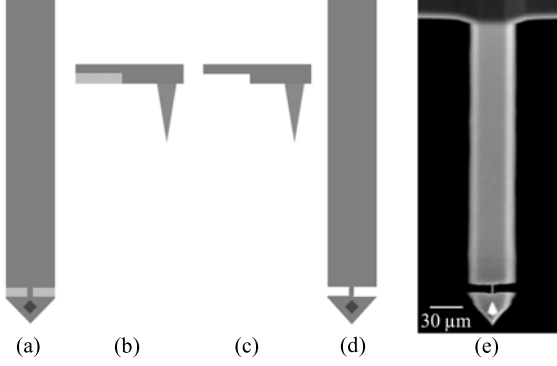


Fig. 6. (a)–(d) Schematics showing the steps in fabrication of the optimized AFM probe. The ion currents employed to machine the probe in steps (a) and (b) was 9.3 nA, while in steps (c) and (d), they were 0.43 nA. (e) Scanning electron micrograph of the fabricated probe.

were not perfectly colocated on the photodetector, the resulting voltage offsets $V_{ox}(y_2), V_{oy}(y_2)$ of the channel y_2 relative to y_1 were compensated before employing it for measurement of angular deformation [see Fig. 5(b)].

2) *Design and Fabrication of the Optimized AFM Probe:* The geometry of the optimized probe was designed to ensure that its dimensions were close to the limits derived in Section II-B2. Table I summarizes the dimensions of the probe along with the resulting compliances at the points y_1 and y_2 .

It is seen from Table I that $c_{\theta y}(y_2)/c_{\theta y}(y_1) \ll c_{\theta z}(y_2)/c_{\theta z}(y_1)$ in accordance with the design guidelines. It is worth noticing, however, that the ratio $c_{\theta z}(y_2)/c_{\theta z}(y_1)$ is 0.21, which differs from the optimal value of 1. The reasons for the difference included considerations of the ability to machine the probe, and the lower limit imposed on ℓ_0 by the size of the laser spot at the location y_1 on the probe.

The optimized AFM probe was fabricated starting from a conventional Silicon probe (All-in-One Cantilever B, Budget Sensors) by means of focused ion beam milling (Helios NanoLab 600i, FEI). Fig. 6(a)–(d) summarizes the important steps in the fabrication of the probe. In the first and second steps [see Fig. 6(a), (b)], coarse machining was performed to remove material and, thereby, reduce the width and thickness to approximately their final dimensions. In the third and fourth steps [see Fig. 6(c), (d)], fine machining was performed using small ion current to bring the probe to its final dimensions. Fig. 6(e) shows a scanning electron micrograph of the fabricated probe.

B. Measurement of 3-D Tip-Sample Interaction Forces

Measurement of 3-D tip-sample forces using the developed system was performed in three steps. First, the angular sensitivities of the probing system at the two measurement locations were calibrated. Next, the dimensions of the probe were employed to determine the compliance matrix \mathbf{C}_θ of the probe, given by (6). Finally, (7) was employed to obtain the 3-D tip-sample forces. It is worth mentioning that in the proposed calibration strategy, the error in measurement of forces is directly related to the error in measurement of the dimensions of the probe and of the positions of the laser spots. Thus, care was taken to precisely measure the probe dimensions by means of a scanning electron microscope, and the position of the laser spots from the micrographs of the setup.

In this section, the procedure employed to calibrate the sensitivity is first described, followed by the measurement of 3-D forces.

1) *Calibration of the Angular Sensitivities of the Measurement System:* The angular sensitivities $k_{phx}(y_1), k_{phy}(y_1), k_{phx}(y_2)$, and $k_{phy}(y_2)$ were calibrated at the start of each experiment. In the adopted strategy, the sensitivities $k_{phx}(y_1), k_{phx}(y_2)$ were calibrated first, followed by $k_{phy}(y_1), k_{phy}(y_2)$.

In order to perform calibration, a hard flat sample with a homogeneous surface, such as freshly cleaved Muscovite mica, was first mounted on a goniometer stage such that its surface was oriented parallel to the plane of the probe. To calibrate $k_{phx}(y_1), k_{phx}(y_2)$, the tip was pressed down along the surface normal of the sample and the changes in $V_y(y_i)$ were recorded for a specified change Δz in the deflection of the probe both during approach and retraction from the sample. If $\Delta V_{yap}(y_i)$ and $\Delta V_{yrt}(y_i)$ represent the corresponding change in deflection signals during approach and retraction, respectively, the angular sensitivities $k_{phx}(y_i)$ at the measurement location $y_i (i = 1, 2)$ can be derived to be (Appendix)

$$k_{phx}(y_i) = \frac{\Delta \bar{V}_y(y_i)}{\Delta z} \frac{c_z(y_i)}{c_{\theta z}(y_i)} \quad (23)$$

where $\Delta \bar{V}_y(y_i) = [\Delta V_{yap}(y_i) + \Delta V_{yrt}(y_i)]/2$, and $c_z(y_i)$ represent the linear compliance of the probe to a force f_z applied at the tip, and are given by

$$c_z(y_i) = \int_0^{y_i} c_{\theta z}(y) dy. \quad (24)$$

The calibrated constants $k_{phx}(y_1), k_{phx}(y_2)$ enable determination of f_y and f_z independently. Thus, the measurements can be employed to determine the coefficient of friction μ of the sample by scanning the surface of the sample along the Y -axis with different Z -forces f_z , and determining the corresponding frictional forces f_y . If Δf_y represents the change in the measured frictional force for a change Δf_z in the Z -force, the coefficient of friction μ is given by

$$\mu = \frac{\Delta f_y}{\Delta f_z}. \quad (25)$$

Calibration of the constants $k_{phy}(y_1), k_{phy}(y_2)$ can be performed by employing standard techniques already reported in

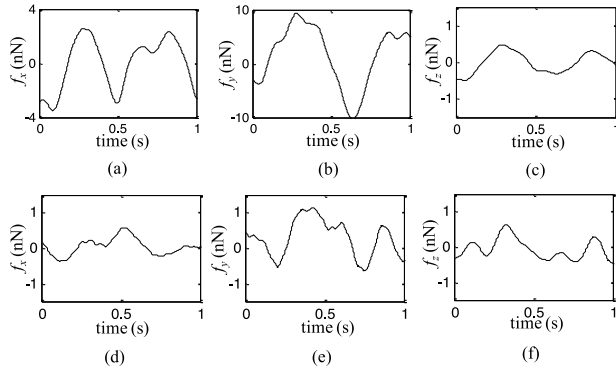


Fig. 7. (a)–(c) Measured noise in force estimates f_x , f_y , f_z , respectively, for a conventional probe. (d)–(f) Measured noise in force estimates f_x , f_y , f_z , respectively, for the optimal probe. In both cases, the measurement bandwidth was 10 Hz.

the literature [25]–[27]. Here, the calibration is performed by equating the coefficient of friction obtained by scanning the sample surface along the Y -axis to that along the X -axis. It is worth noticing that this method is not sufficiently general, because it assumes a symmetric tip and an isotropic sample surface and, therefore, can be considered a “quick-and-dirty” method. If $\Delta V_x(y_i)$ represent the changes in $V_x(y_i)$ due to a change Δf_z in the Z -force, the constants $k_{phy}(y_i)$ ($i = 1, 2$) are obtained to be (Appendix)

$$k_{phy}(y_i) = \frac{\Delta V_x(y_i)}{\mu \Delta f_z c_{\theta x}(y_i)}. \quad (26)$$

The proposed calibration strategy was employed to calibrate the angular sensitivities at y_1 and y_2 for the fabricated optimized probe and a conventional rectangular probe (PPP-XYCONTR, Nanosensors, stiffness 0.2 N/m). For the conventional probe, the measurements were made at the optimal locations described in Section II-B1, viz., $\tilde{y}_1 = 1$ and $\tilde{y}_2 \approx 0.5$. Subsequently, the noise in estimation of forces along X -, Y - and Z -axes were obtained both for the optimized probe and the conventional probe. Fig. 7(a)–(c) shows the noise along the three axes for the conventional probe, while Fig. 7(d)–(f) shows the noise for the optimized probe. It is seen that the noise in force estimates are nearly identical along all the three axes for the optimized probe, while they are significantly higher along X - and Y -axes compared to Z -axis for a conventional probe. The resulting standard deviations in the measured noise were found to be $\sigma_{f_x} = 1.9 \text{ nN}$, $\sigma_{f_y} = 5.6 \text{ nN}$, $\sigma_{f_z} = 0.28 \text{ nN}$ for the conventional probe, while for the optimized probe they were $\sigma_{f_x} = 0.23 \text{ nN}$, $\sigma_{f_y} = 0.64 \text{ nN}$, $\sigma_{f_z} = 0.25 \text{ nN}$.

2) Measurement of 3-D Forces Using the Optimized AFM Probe: To evaluate direct measurement of 3-D forces with the optimized AFM probe, the angular sensitivities of the probe at the two measurement locations y_1 and y_2 were first calibrated. Subsequently, the surface of a freshly cleaved Muscovite mica sample was scanned along X - and Y -axes at different normal loads, with velocities in the range 125–250 nm/s, and the resulting frictional forces applied at the tip were obtained by the measurement system. To minimize the effect of measurement

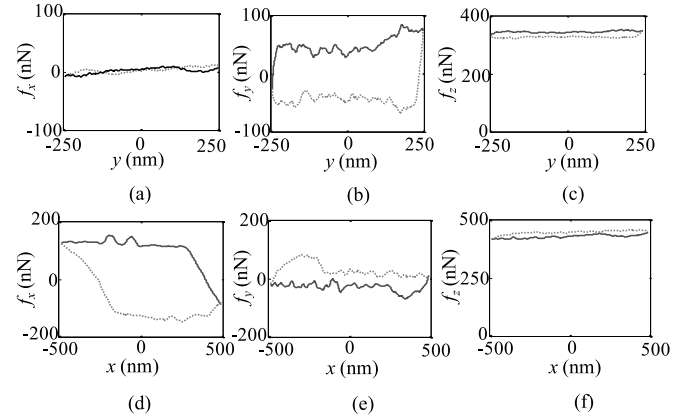


Fig. 8. (a)–(c) Measured forces f_x , f_y , f_z when the sample was displaced along Y -axis relative to the tip. (d)–(f) Measured forces f_x , f_y , f_z when the sample was displaced along X -axis. In both cases, the solid lines represent the behavior for forward motion, while the dashed lines represent the behavior for reverse motion. The sensitivities were calibrated to be $k_{phx}(y_1) = 0.81 \text{ V/mrad}$, $k_{phy}(y_1) = 1.2 \text{ V/mrad}$, $k_{phx}(y_2) = 2.6 \text{ V/mrad}$, and $k_{phy}(y_2) = 2.6 \text{ V/mrad}$.

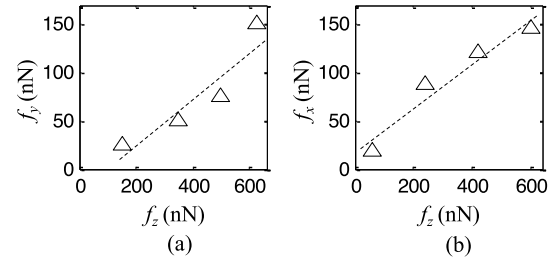


Fig. 9. Measured average friction forces (a) f_y and (b) f_x as a function of the average force f_z .

noise and structural vibrations on the measured forces in both cases, a 10 Hz low-pass filter cascaded with a 12.5-Hz notch filter was employed.

Fig. 8(a)–(c) shows the measured forces f_x , f_y , and f_z when the sample was displaced along the Y -axis relative to the tip, while Fig. 8(d)–(f) shows the measured forces when it was displaced along the X -axis. It is seen from both the figures that significant changes in the magnitude of the measured force occur primarily along the axis of displacement. Further, when the direction of motion is reversed, the measured force along this direction also changes sign and, thereby, demonstrates the hysteretic-behavior characteristic of friction effects [28].

The sample was displaced along Y - and X -axes relative to the tip at three other values of the mean normal load (f_z). In each case, the mean frictional forces, viz., f_y , f_x , respectively, were recorded. Fig. 9(a), (b) plots the mean values of f_y , f_x as a function of the mean values of f_z . It is seen from the figure that in both cases, the friction forces exhibit nearly linear dependence on f_z . The slopes of the linear least square fits in both cases yield the coefficient of friction to be 0.24. This is in general agreement with the coefficient of friction reported for Muscovite mica in the literature [21], [29]–[31]. However, it is worth mentioning that the linear dependence of friction on

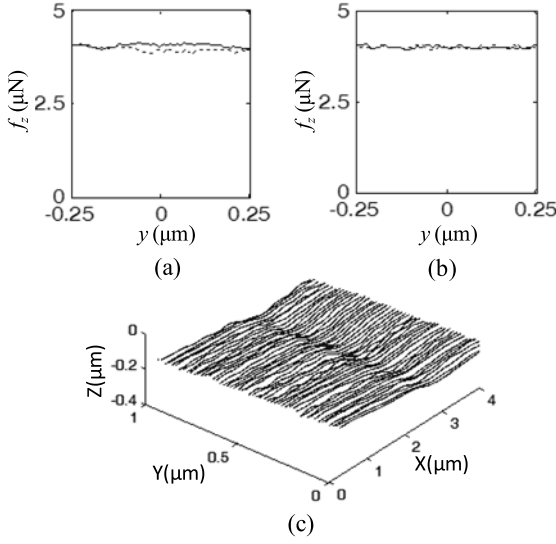


Fig. 10. Measured force f_z during forward- and reverse-direction scans (a) without feedback control and (b) with feedback control. The solid lines represent scan in the forward direction, while the dashed lines represent the scans in the reverse direction. The PI-controller gains were set to be $K_P = 4$, $K_I = 220$. (c) AFM scan showing a groove of depth about 25 nm made on the surface of PMMA.

normal force is only an approximate description. In general, the friction forces at the nanometer scale are nonlinear functions of the normal load [32], [33], and for single asperity contacts, interfacial shear can be employed to better model these forces [33]–[35].

C. Real-Time Force Control Using the Measurement System

The ability of the measurement system to obtain tip-sample forces in real-time enables its use for control of the interaction forces. To demonstrate its applicability, a feedback control system was designed to regulate the Z-component of the measured force f_z at a set point f_{z0} as the sample was scanned along the Y-axis. The experiments were performed on freshly cleaved Muscovite mica with a rectangular probe (All-in-One Cantilever C, Budget Sensors, stiffness 10.2 N/m), and the probe deformation was measured at the optimal locations discussed in Section II-B1, i.e., $\tilde{y}_1 = 1$ and $\tilde{y}_2 \approx 0.5$. The measured force f_z was regulated at the set point $f_{z0} = 4 \mu\text{N}$ by means of a proportional-integral (PI) controller. Fig. 10(a), (b) compares the variation in the measured f_z with feedback control to that without control during the scan. The resulting mean difference in f_z between forward and reverse motions is found to be about 1.32% without feedback control, while with feedback control, it is seen to be suppressed to about 0.013%. It is worth noticing that in conventional AFM systems, the force f_z cannot be measured independent of the longitudinal force f_y . Thus, the developed system can be employed when the scanning-trajectory results in significant f_y , such as in the spiral or Lissajous scans [36]–[38] that find applications in high-speed AFM.

Subsequently, the developed control system was employed for performing force-controlled nanoscribing on a PMMA sample. The PMMA was spin coated on a Silicon substrate to a nominal

height of 100 nm. A rectangular probe (MPP33120, Bruker, stiffness 4.5 N/m) was docked on the sample, and the force f_z was controlled at a set point of $f_{z0} = 10 \mu\text{N}$ as the sample was scribed along the Y-axis. Subsequently, the same area was scanned by employing a much lesser set point force of $f_{z0} = 0.5 \mu\text{N}$. Fig. 10(c) shows the AFM scan and reveals the groove, of depth about 25 nm, made by the probe on the surface of PMMA.

IV. CONCLUSION

This paper reported the design and evaluation of a measurement system for direct real-time measurement of 3-D tip-sample interaction forces in AFM. The proposed strategy was based on measurement of the deflection of the AFM probe at two points on it. The optimal positions for making the measurements were determined for a conventional probe. Further, a new optimized geometry was proposed for the probe that enables measurement of all three forces with identical sensitivity and nearly identical resolution. The measurement system and the optimized probe were both fabricated. A strategy was proposed to calibrate the sensitivity of the measurement system to tip-sample forces, and the system was subsequently evaluated by scanning a sample with the optimized AFM probe. The evaluation validated the accuracy of the measurement system and the minimal effect of cross-talk. Finally, the developed real-time measurement system was employed as part of a feedback control system to regulate the normal force and to perform force-controlled scribing of a groove on the surface of PMMA. The proposed design for the measurement system enables it to also measure dynamic tip-sample forces and to be easily retrofitted into existing AFM systems. Thus, as a consequence of the reported features of the developed system, it benefits a variety of applications in both quasi-static and dynamic mode AFM, including force spectroscopy, nanometrology, and nanomanipulation.

APPENDIX

This section describes the calibration of the angular measurement sensitivities at the two measurement locations y_1 and y_2 on the probe.

In order to calibrate the sensitivities $k_{phx}(y_1)$, $k_{phx}(y_2)$, the probe is pressed down on a hard flat sample, whose surface normal is oriented perpendicular to the probe. The resulting Y- and Z-forces f_y , f_z experienced by the tip for a deflection z of the AFM tip satisfy

$$z = c_z(y_1)f_z + c_y(y_1)f_y \quad (27)$$

where $c_z(y_1)$, $c_y(y_1)$ represent the linear compliances of the probe at the measurement location y_1 . As the probe is pressed down on the sample, the tip tends to translate along the positive Y-axis and, thus, experiences friction force given by $f_y = -\mu N$, where N is the sum of f_z and the adhesive force f_{adh} between the tip and the sample, i.e., $N = f_z + f_{adh}$. As the probe is retracted from the sample the tip translates along the negative Y-axis and, thus, experiences friction force $f_y = +\mu N$. Thus, from (27), the Z-force during the approach and retract, viz.,

f_{zap}, f_{zrt} are given by

$$\begin{aligned} f_{zap} &= \frac{z + \mu c_y(y_1) f_{adh}}{c_z(y_1) - \mu c_y(y_1)} \\ f_{zrt} &= \frac{z - \mu c_y(y_1) f_{adh}}{c_z(y_1) + \mu c_y(y_1)}. \end{aligned} \quad (28)$$

Since typically $\mu < 1$, it is seen from (28) that for a change Δz in the position of the tip, the corresponding change in the mean force $\bar{f}_z = (f_{zap} + f_{zrt})/2$ satisfies

$$\Delta \bar{f}_z \approx \frac{\Delta z}{c_z(y_1)}. \quad (29)$$

Further, if $\theta_{xap}(y_i), \theta_{xrt}(y_i)$ represent the corresponding angular deformations of the probe about the X-axis at the measurement locations $y_i (i = 1, 2)$ during approach and retraction, respectively, (6) can be employed to demonstrate that the change in average values of the angular deformations $\bar{\theta}_x(y_i) = (\theta_{xap}(y_i) + \theta_{xrt}(y_i))/2$ are related to the forces as

$$\Delta \bar{\theta}_x(y_i) = c_{\theta z}(y_i) \Delta \bar{f}_z. \quad (30)$$

Finally, noticing that $\theta_x(y_i) = V_y(y_i)/k_{phx}(y_i)$, (29) and (30) can be employed to obtain the constants $k_{phx}(y_i) (i = 1, 2)$ as

$$k_{phx}(y_i) = \frac{\Delta \bar{V}_y(y_i)}{\Delta z} \frac{c_z(y_i)}{c_{\theta z}(y_i)} \quad (31)$$

where $\Delta \bar{V}_y(y_i) = [\Delta V_{yap}(y_i) + \Delta V_{yrt}(y_i)]/2$.

In order to calibrate $k_{phy}(y_1), k_{phy}(y_2)$, the probe is pressed down on a sample to apply a force f_z and the sample is subsequently displaced along the X-axis relative to the tip. This causes the tip to experience a friction force $f_x = \mu N$. Thus, the difference in friction force Δf_x experienced by the probe due to a difference Δf_z in the Z-axis force satisfies

$$\Delta f_x = \mu \Delta f_z. \quad (32)$$

Noting, from (2) that $\Delta \theta_y(y_i) = c_{\theta x}(y_i) \Delta f_x$, and that $\Delta \theta_y(y_i) = \Delta V_x(y_i)/k_{phy}(y_i)$, it can be concluded that the constants $k_{phy}(y_i)$ can be obtained to be

$$k_{phy}(y_i) = \frac{\Delta V_x(y_i)}{\mu \Delta f_z c_{\theta x}(y_i)}. \quad (33)$$

REFERENCES

- [1] E. Meyer, "Atomic force microscopy," *Prog. Surf. Sci.*, vol. 41, no. 1, pp. 3–49, Sep. 1992.
- [2] F. J. Giessibl, "Advances in atomic force microscopy," *Rev. Mod. Phys.*, vol. 75, no. 3, pp. 949–983, Jul. 2003.
- [3] A. Weckenmann, G. Peggs, and J. Hoffmann, "Probing systems for dimensional micro- and nano-metrology," *Meas. Sci. Technol.*, vol. 17, pp. 504–509, Jan. 2006.
- [4] M. Sitti, "Survey of nanomanipulation systems," in *Proc. IEEE 1st Conf. Nanotechnol.*, 2001, pp. 75–80.
- [5] H. Ni and X. Li, "Young's modulus of ZnO nanobelts measured using atomic force microscopy and nanoindentation techniques," *Nanotechnology*, vol. 17, no. 14, pp. 3591–3597, Jun. 2006.
- [6] J. Zlatanova, S. M. Lindsay, and S. H. Leuba, "Single molecule force spectroscopy in biology using the atomic force microscope," *Prog. Biophys. Mol. Biol.*, vol. 74, pp. 37–61, 2000.
- [7] D. Fotiadis, S. Scheuring, S. A. Müller, A. Engel, and D. J. Müller, "Imaging and manipulation of biological structures with the AFM," *Micron*, vol. 33, no. 4, pp. 385–397, 2002.
- [8] I. Obataya, C. Nakamura, S. Han, N. Nakamura, and J. Miyake, "Nanoscale operation of a living cell using an atomic force microscope with a nanoneedle," *Nano Lett.*, vol. 5, no. 1, pp. 27–30, 2005.
- [9] G. Dai, H. Wolff, T. Weimann, M. Xu, F. Pohlenz, and H. U. Danzebrink, "Nanoscale surface measurements at sidewalls of nano- and microstructures," *Meas. Sci. Technol.*, vol. 18, pp. 334–341, 2007.
- [10] G. R. Jayanth and C. H. Menq, "Tip motion control and scanning of a reorientable micromanipulator with axially located tip," *IEEE/ASME Trans. Mechatronics*, vol. 17, no. 5, pp. 801–810, Oct. 2012.
- [11] G. R. Jayanth and C. H. Menq, "Two-axis force sensing and control of a reorientable scanning probe," *IEEE/ASME Trans. Mechatronics*, vol. 18, no. 2, pp. 687–696, Apr. 2013.
- [12] M. Sitti and H. Hashimoto, "Controlled pushing of nanoparticles: Modeling and experiments," *IEEE/ASME Trans. Mechatronics*, vol. 5, no. 2, pp. 199–211, Jun. 2000.
- [13] M. Sitti, "Atomic force microscope probe based controlled pushing for nano-tribological characterization," *IEEE/ASME Trans. Mechatronics*, vol. 8, no. 3, pp. 1–7, Sep. 2003.
- [14] C. D. Onal, O. Ozcan, and M. Sitti, "Automated 2-D nanoparticle manipulation using atomic force microscopy," *IEEE Trans. Nanotechnol.*, vol. 10, no. 3, pp. 472–481, May 2011.
- [15] H. Xie and S. Régnier, "Development of a flexible robotic system for multiscale applications of micro/nanoscale manipulation and assembly," *IEEE/ASME Trans. Mechatronics*, vol. 16, no. 2, pp. 266–276, Apr. 2011.
- [16] A. Bolopion, H. Xie, D. S. Haliyo, and S. Régnier, "Haptic teleoperation for 3-D microassembly of spherical Objects," *IEEE/ASME Trans. Mechatronics*, vol. 17, no. 1, pp. 116–127, Feb. 2012.
- [17] H. Kawakatsu and T. Saito, "Scanning force microscopy with two optical levers for detection of deformations of the cantilever," *J. Vac. Sci. Technol. B*, vol. 14, no. 2, pp. 872–876, 1996.
- [18] G. Meyer and N. M. Amer, "Simultaneous measurement of lateral and normal forces with an optical beam deflection atomic force microscope," *Appl. Phys. Lett.*, vol. 57, no. 20, pp. 2089–2091, Nov. 1990.
- [19] B. I. Kim, J. R. Bonander, and J. A. Rasmussen, "Simultaneous measurement of normal and friction forces using a cantilever-based optical interfacial force microscope," *Rev. Sci. Instrum.*, vol. 82, no. 5, pp. 053711–1–053711–5, May 2011.
- [20] G. Li, N. Xi, M. Yu, and W. K. Fung, "Development of augmented reality system for AFM-based nanomanipulation," *IEEE/ASME Trans. Mechatronics*, vol. 9, no. 2, pp. 358–365, Jun. 2004.
- [21] C. D. Onal and M. Sitti, "Teleoperated 3-D force feedback from the nanoscale with an atomic force microscope," *IEEE Trans. Nanotechnol.*, vol. 9, no. 1, pp. 46–54, Jan. 2010.
- [22] G. C. Ratcliff, D. A. Erie, and R. Superfine, "Photothermal modulation for oscillating mode atomic force microscopy in solution," *Appl. Phys. Lett.*, vol. 72, no. 15, pp. 1911–1913, Apr. 1998.
- [23] S. Timoshenko, *Strength of Materials: Part-I Elementary Theory and Problems*. New Delhi, India: CBS Publishers & Distributors Pvt. Ltd., 2002.
- [24] S. W. Smith, *The Scientist and Engineer's Guide to Digital Signal Processing*, 2nd ed. San Diego, CA, USA: California Techn. Publishing, 1999, pp. 11–34.
- [25] D. F. Ogletree, R. W. Carpick, and M. Salmeron, "Calibration of frictional forces in atomic force microscopy," *Rev. Sci. Instrum.*, vol. 67, no. 9, pp. 3298–3306, Sep. 1996.
- [26] U. D. Schwarz, P. Köster, and R. Wiesendanger, "Quantitative analysis of lateral force microscopy experiments," *Rev. Sci. Instrum.*, vol. 67, no. 7, pp. 2560–2567, Jul. 1996.
- [27] Y. D. Yan, S. Dong, and T. Sun, "3-D force components measurement in AFM scratching tests," *Ultramicroscopy*, vol. 105, pp. 62–71, 2005.
- [28] J. A. Ruan and B. Bhushan, "Atomic-scale friction measurements using friction force microscopy: Part I—General principles and new measurement techniques," *J. Tribology*, vol. 116, no. 2, pp. 378–388, Apr. 1994.
- [29] P. Attard, J. Stiernstedt, and M. W. Rutland, "Measurement of friction coefficients with the atomic force microscope," *J. Phys., Conf. Ser.*, vol. 61, no. 1, pp. 51–55, 2007.
- [30] A. Srivastava, "Dynamic friction measurement and modeling at the micro/nano scale," Ph.D. dissertation, Dept. Mech. Eng., Univ. California, Santa Barbara, CA, USA, Sep. 2006.
- [31] J. Hu, X.-D. Xiao, D. F. Ogletree, and M. Salmeron, "Atomic scale friction and wear of mica," *Surf. Sci.*, vol. 327, no. 3, pp. 358–370, 1995.

- [32] E. Gnecco, R. Bennewitz, T. Gyalog, C. Loppacher, M. Bammerlin, E. Meyer, and H.-J. Güntherodt, "Velocity dependence of atomic friction," *Phys. Rev. Lett.*, vol. 84, no. 6, pp. 1172–1175, Feb. 2000.
- [33] R. W. Carpick and M. Salmeron, "Scratching the surface: Fundamental investigations of tribology with atomic force microscopy," *Chem. Rev.*, vol. 97, pp. 1163–1194, 1997.
- [34] A. M. Homola, J. N. Israelachvili, P. M. McGuiggan, and M. L. Gee, "Fundamental experimental studies in tribology: The transition from 'Interfacial' friction of undamaged molecularly smooth surfaces to 'normal' friction with wear," *Wear*, vol. 136, pp. 65–83, 1990.
- [35] H. Yoshizawa, Y.-L. Chen, and J. Israelachvili, "Fundamental mechanisms of interfacial friction. 1. Relation between adhesion and friction," *J. Phys. Chem.*, vol. 97, pp. 4128–4140, 1993.
- [36] I. A. Mahmood and S. O. R. Moheimani, "Fast spiral-scan atomic force microscopy," *Nanotechnology*, vol. 20, pp. 365503-1–365503-4, Aug. 2009.
- [37] T. Tuma, J. Lygeros, V. Kartik, A. Sebastian, and A. Pantazi, "High-speed multiresolution scanning probe microscopy based on Lissajous scan trajectories," *Nanotechnology*, vol. 23, pp. 185501-1–185501-9, Apr. 2012.
- [38] M. S. Rana, H. R. Pota, and I. R. Petersen, "Performance of sinusoidal scanning with MPC in AFM imaging," *IEEE/ASME Trans. Mechatronics*, vol. 20, no. 1, pp. 73–83, Feb. 2015.



R. Sri Muthu Mrinalini received the B.E. degree in electronics and instrumentation engineering from Anna University, Tiruchirappalli, India, in 2011. She is currently working toward the Ph.D. degree at the Department of Instrumentation and Applied Physics, Indian Institute of Science, Bangalore, India.

Her current research interests include nanometrology, scanning probe microscopy, optical instrumentation, actuation, and control of micromechanical systems.



R. Sriramshankar received the B.Tech degree in instrumentation and control engineering from the National Institute of Technology, Tiruchirappalli, India, in 2010. He is currently working toward the Ph.D. degree at the Department of Instrumentation and Applied Physics, Indian Institute of Science, Bangalore, India.

His current research interests include scanning probe microscopy, optical instrumentation, and dynamics of micromechanical systems.



G. R. Jayanth received the B.Tech degree from the Indian Institute of Technology-Madras, Chennai, India, in 2002, and the M.S. and Ph.D. degrees both in mechanical engineering from The Ohio State University, Columbus, OH, USA, in 2004 and 2008, respectively.

Since 2010 he has been an Assistant Professor at the Department of Instrumentation and Applied Physics with the Indian Institute of Science, Bangalore, India. His current research interests include nanometrology, scanning probe microscopy, and dynamics and control of micromechanical devices.